

Lawrence Berkeley National Laboratory

LBL Publications

Title

Pioneering Microporous Layers for Proton-Exchange-Membrane Water Electrolyzers via Tape Casting

Permalink

<https://escholarship.org/uc/item/6gx220db>

Journal

Journal of The Electrochemical Society, 171(6)

ISSN

0013-4651

Authors

Lee, Jason K
Lau, Grace Y
Shen, Fengyu
[et al.](#)

Publication Date

2024-06-03

DOI

10.1149/1945-7111/ad54f1

Copyright Information

This work is made available under the terms of a Creative Commons Attribution License, available at <https://creativecommons.org/licenses/by/4.0/>

Peer reviewed

OPEN ACCESS

Pioneering Microporous Layers for Proton-Exchange-Membrane Water Electrolyzers via Tape Casting

To cite this article: Jason K. Lee *et al* 2024 *J. Electrochem. Soc.* **171** 064505



View the [article online](#) for updates and enhancements.

You may also like

- [Investigation of Charge-Transfer and Mass-Transport Resistances in PEMFCs with Microporous Layer Using Electrochemical Impedance Spectroscopy](#)
Dzmitry Malevich, Ela Halliop, Brant A. Peppley et al.
- [Catalyst Layer Resistance and Utilization in PEM Electrolysis](#)
Elliot Padgett, Guido Bender, Andrew Haug et al.
- [Numerical Study of the Impact of Two-Phase Flow in the Anode Catalyst Layer on the Performance of Proton Exchange Membrane Water Electrolyzers](#)
M. Moore, M. Mandal, A. Kosakian et al.



Pioneering Microporous Layers for Proton-Exchange-Membrane Water Electrolyzers via Tape Casting

Jason K. Lee,^{1,2,3,z}  Grace Y. Lau,¹ Fengyu Shen,¹  Anyka Bergeson-Keller,¹ Xiong Peng,¹ and Michael C. Tucker^{1,z}

¹Energy Technology Area, Lawrence Berkeley National Laboratory, Berkeley, California 94720, United States of America

²Department of Mechanical Engineering, University of Victoria, Victoria, BC V8P 5C2, Canada

³Institute for Integrated Energy Systems (IESVic), University of Victoria, Victoria, BC V8P 5C2, Canada

The imperative shift towards decarbonization necessitates the production of clean hydrogen through water electrolysis, powered by renewable energy sources. Among electrolyzer technologies, proton-exchange-membrane (PEM) systems emerge as a promising option for large-scale hydrogen generation due to their modular design and rapid response, aligning well with the intermittency of renewable energy. In this study, we employ a tape casting method to fabricate microporous layers (MPLs), both as a single layer and as a bilayer over commercial porous transport layers (PTLs), to further enhance performance of water electrolyzers. We demonstrate that microporous layers require adequate pore sizes to facilitate gas removal, preventing gas flooding and preserving electrolyzer performance. Our single layer microporous layers exhibit lower overpotentials compared to commercial sintered Ti PTLs by 142 mV at 4 A·cm⁻². Moreover, we show that having an effective microporous layer enhances electrolyzer performance irrespective of the substrate used, offering avenues for cost reduction. We also investigate novel PTL structures with reduced tortuosity and integrated MPL fabricated via phase inversion tape casting, resulting in a performance enhancement of 92 mV. Our findings unravel the critical role of microporous layer structures and their impact on electrolyzer performance.

© 2024 The Author(s). Published on behalf of The Electrochemical Society by IOP Publishing Limited. This is an open access article distributed under the terms of the Creative Commons Attribution 4.0 License (CC BY, <http://creativecommons.org/licenses/by/4.0/>), which permits unrestricted reuse of the work in any medium, provided the original work is properly cited. [DOI: 10.1149/1945-7111/ad54f1]



Manuscript submitted March 5, 2024; revised manuscript received May 2, 2024. Published June 14, 2024.

Supplementary material for this article is available [online](#)

The continuous increase in global temperature has escalated the need to transition towards zero-emission technologies, and hydrogen is emerging as an ideal solution for decarbonization of hard-to-abate sectors.¹ Hydrogen can be utilized in fuel cells for such sectors as transportation² and industrial power.^{3–7} However, the caveat is that decarbonization is contingent upon the production of hydrogen itself adhering to environmentally friendly practices. Conventional hydrogen production today relies heavily on hydrocarbon reforming, which admittedly co-produces carbon dioxide as a byproduct of hydrogen production.⁸ A better approach for hydrogen production is electrolysis, where electrical energy is used to dissociate water into hydrogen and oxygen. When an electrolyzer is powered with renewables, it is capable of producing hydrogen at near zero emissions. Despite the promise, the high cost of electrolyzed hydrogen impedes market penetration, as only 2% of the hydrogen produced today originates from electrolysis compared to 76% stemming from reforming and 22% from coal gasification.⁹ Cost reduction for electrolyzed hydrogen is imperative to widespread adoption of hydrogen technologies.

Among various electrolyzer types, proton-exchange-membrane (PEM) water electrolyzers exhibit the greatest potential for expanding hydrogen production. These electrolyzers provide rapid response times, making them well-suited for integration with intermittent renewable energy sources. Additionally, their compact design facilitates the scalability of this technology.¹⁰ In a PEM electrolyzer, reactant liquid water is fed from the anode flow channel to the titanium porous transport layer (PTL), which uniformly distributes liquid water over the catalyst layer. With current applied, the anode electrode catalyzes the oxygen evolution reaction, and the cathode electrode catalyzes the hydrogen evolution reaction. Previous literature^{11–18} identified that the interface between the catalyst layer and the porous transport layer (CL/PTL interface) strongly influences the performance of the PEM electrolyzers. Increased contact at the CL/PTL interface promotes electrical contact in the catalyst layer, improving catalyst utilization while also preventing deformation of the catalyst layer and membrane into

the interface.^{11,12} However, Peng et al. have shown that mass transport must also be considered when choosing the appropriate PTL, as high mass transport overpotential occurs for dense PTLs.¹⁸ Both modelling efforts and experimental efforts indicate the need for a supporting interface layer for electrolyzers, similar to microporous layers (MPLs) used in fuel cells.^{19–26}

PTLs used in PEM water electrolyzers are typically fabricated from titanium, as the highly corrosive environment of the anode compartment limits the material selection.¹⁰ However, processing titanium remains complicated and costly because of its high melting temperature and chemical affinity with atmospheric gases.²⁷ Previous efforts have been made to fabricate PTLs either starting from commercial Ti structures²⁸ or building from scratch,^{22–24} yet high cost and difficulty in acquiring precise control over the PTL structure remain. Lee et al.²⁸ showed that patterned through-pores added in the PTL accelerate gas removal by reducing tortuosity, thereby improving mass transport during operation. Other efforts include vacuum plasma spray deposition of a support layer on commercial and mesh-type PTLs.^{21,23–26} Similarly, Schuler et al.^{22,29} showed that a Ti MPL improves electrolyzer performance, and the CL/PTL interface is a crucial MPL property. However, the MPLs reported to date did not have tunable pore size at the CL/PTL interface, which is a key parameter to find the optimal MPL structure.

Previously, our work has demonstrated that tape casting is a facile and scalable method for fabricating PTLs, with ease in controlling pore structures using pore formers.³⁰ Tape casting is a well-established technique for making sheets of ceramics and metals from powder.³¹ As a roll-based process, it has high throughput and is very scalable, and commercial equipment is readily available from many manufacturers. In this work, we explore the tape casting method to fabricate advanced MPLs for high performance PEM water electrolyzers (Fig. 1). We first investigate the feasibility of fabricating a single layer MPL. Then, we down select the best MPL and form a bilayer structure that resembles the MPL used in fuel cells. Lastly, we explore the use of phase inversion tape casting method to fabricate customized PTLs that exhibit simultaneous high contact area in an MPL layer integrated onto a low tortuosity support layer. Our findings on fabrication of MPLs through tape casting

^zE-mail: jasonklee@uvic.ca; mctucker@lbl.gov

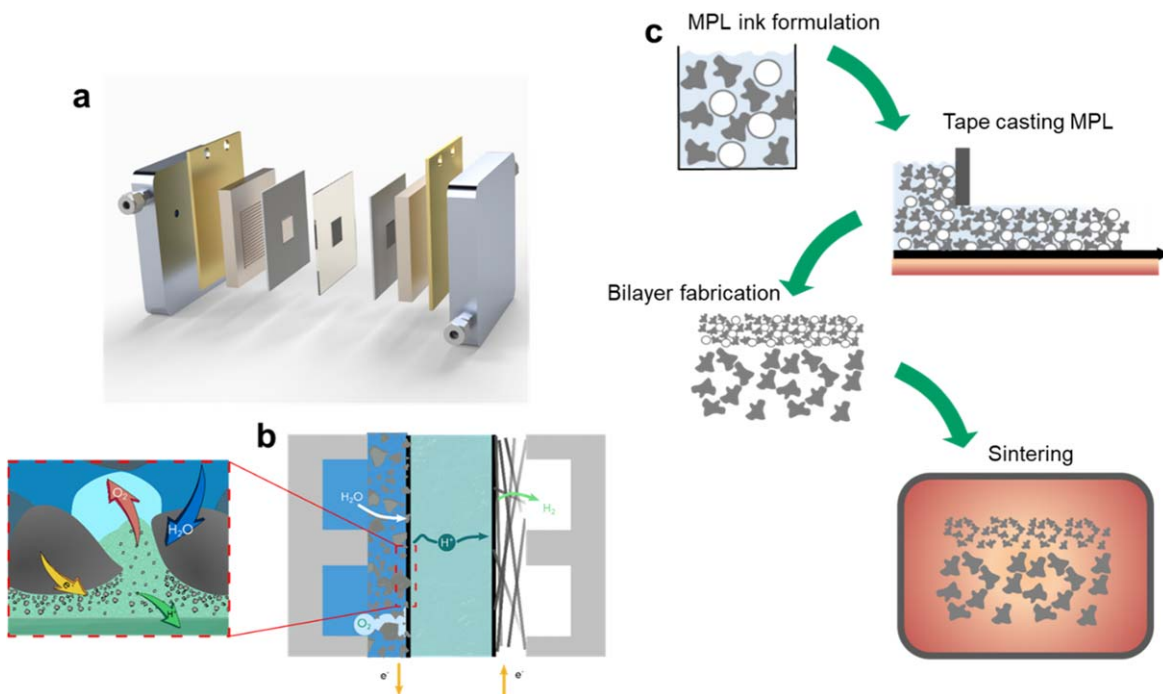


Figure 1. Schematic of the proton-exchange-membrane water electrolyzer and tape casting process used to fabricate microporous layers. (a) Exploded view of testing hardware components, and (b) the functions of each anode component. (c) Schematic summarizing the key steps in the tape casting process to fabricate MPLs.

provides a new paradigm in designing PTLs for PEM water electrolyzers.

Experimental Methods

Single layer tape casting and multi-layer lamination.—Tape casting closely followed the process reported previously.³⁰ Commercial titanium powder (Alfa Aesar –325 mesh ($<44\ \mu\text{m}$), Alfa Aesar –200 mesh ($<74\ \mu\text{m}$), or U.S. Nano $5\ \mu\text{m}$) and polymethyl methacrylate (PMMA) poreformer (Sunjin 10, 30 or $60\ \mu\text{m}$) were used, and images of the powders are shown in Fig. S1. Slurries were prepared by mixing the powders with 2.5 wt% polyvinyl butyral binder (PVB, Spectrum Chemical), 2.5 wt% polyethylene glycol surfactant (Sigma Aldrich, MW 300), and 30 wt% ethanol solvent (Sigma Aldrich). The slurry was milled for 24 h on a jar roller mill (US Stoneware RMV 755). Slurries were cast into tapes on silicone-treated polyethylene terephthalate (Si-PET) film using an adjustable-gap doctor blade (Paul N. Gardner Company, Inc.) and a lab caster (MSK-AFA IIID Automatic Thick Film Coater, MTI) with the casting bed at $40\ ^\circ\text{C}$. Selection of cast thickness to achieve a desired final sintered thickness is illustrated in Fig. S2. The tapes were dried on the casting bed for 10 min and at room temperature for 24 h.

In some cases, multiple tapes were laminated together to produce a bi-layer MPL/PTL structure. Lamination was carried out at $75\ ^\circ\text{C}$ and 20.7 MPa for 10 min using a uniaxial press with heated platens (Carver). Commercially-available sintered Ti PTLs in powder (Mott 1100 Series, Mott Corp.) and fiber (2GDL10–0.25, NV Bekaert SA) forms were used as substrates.

Phase inversion.—Phase inversion tape casting followed a process we reported previously for ceramic powder.³² Ti powder (U.S. Nano $5\ \mu\text{m}$, 10 g), QPAC 40 binder (Empower Materials, 0.8 g), and N-Methyl-2-pyrrolidone solvent (5.8 g) were added to a Teflon bottle with 30 g zirconia balls, and ball milled overnight. Separately, PMMA powder (Kowa Soken MX-300, 1 g), QPAC 40

binder (Empower Materials, 0.8 g), and N-Methyl-2-pyrrolidone solvent (7 g) were similarly mixed. The Ti slurry was then tape cast onto bare PET film, and the PMMA slurry was immediately cast on top of it with a second pass of the doctor blade with the blade gap increased. Instead of drying, the tape was immediately soaked in a bath of de-ionized water to incur phase inversion between the water and solvent (tapes) phases. The water bath was held at either $50\ ^\circ\text{C}$ in an oven, or at $0\ ^\circ\text{C}$ in a tray of ice water. After exchange between the water phase and the solvent phase was complete ($\sim 20\ \text{min}$), the tape was dried overnight at room temperature. Upon sintering, the sacrificial PMMA layer burns off and reveals the large pores formed in the Ti layer. Before developing this recipe, standard phase inversion binders were used unsuccessfully, as shown in Fig. S3.

Sintering.—Tapes were peeled from the Si-PET substrate, and sintered on a zirconia plate (MTI Corporation, 8% YSZ) in a tube furnace (Lindberg Blue, alumina tube) with flowing ultra-high purity argon (99.999%). Samples were debinded at $400\ ^\circ\text{C}$ for 2 h during ramp-up, and sintered at $1050\ ^\circ\text{C}$ for 2 h (except where noted). Heating and cooling ramps were $3\ ^\circ\text{C}\ \text{min}^{-1}$. The resulting porous titanium sheet was laser-cut to $5\ \text{cm}^2$ size (fiber laser cutter, Full Spectrum Laser), cleaned with etching solution (Multi-etch), and coated with approximately 40 nm of platinum at the CL/titanium interface to enhance electrical contact and suppress oxidation (RF sputter, AJA International Inc.).

Imaging.—Powders and sintered samples were imaged using scanning electron microscopy (SEM). Sintered samples were embedded in epoxy (Struers, EpoFix), cross-sectioned with a diamond saw (Buehler), and smoothed on a metallurgical polishing table (Buehler) using silicon carbide polishing papers (Struers, grit sizes 240, 320, 400, 600, 800, and 1200). The samples were polished with aqueous diamond suspensions on polishing cloth (Allied High Technology Products, 3, 1, and $0.05\ \mu\text{m}$ particles). The cross-sectioned samples were sputtered with a thin layer of gold prior to imaging. A JEOL 7500 F SEM was used for imaging.

Thermogravimetric analysis.—Binder burnout in argon was analyzed using a thermogravimetric analyzer system (Perkin Elmer, TGA 4000). Each binder candidate (20 mg) was placed in a ceramic crucible and heated to 900 °C at a ramp rate of 3 °C·min⁻¹ with ultra-high purity argon purge (99.999%, 20 ml·min⁻¹).

Preparation of the catalyst coated membranes and electrolyzer cell testing.—Catalyst coated membranes used for electrolyzer experiments were fabricated via ultrasonic spray coating. Commercial iridium oxide catalyst (TKK ECL-0110 SA = 100, Tanaka) mixed with Nafion ionomer solution (5 wt%, Ion Power D521) at ionomer-to-catalyst ratio of 0.116, water, ethanol, and n-propanol at a ratio of 1:1:2 by volume were used to make anode catalyst ink. For cathode catalyst ink, commercially available platinum supported by carbon (TEC10V50E 46.3% Pt, Tanaka), Nafion ionomer solution (5 wt%, Ion Power D521) at ionomer to catalyst ratio of 0.45, water, and n-propanol, were mixed at a ratio of 1:1 by volume. Before spray coating, the anode catalyst ink underwent sonication with a horn sonicator (CEX500, Cole-Parmer) at 38% power for 30 min, and the cathode catalyst ink underwent sonication with a bath sonicator for 30 min to prevent displacement of Pt particles from carbon support. The ink volume was kept constant to ensure the consistency of the coating throughout the experiments. The 178 μm thick Nafion membrane (N117, Ion Power) was used as the substrate. Prior to coating, the membranes were soaked in boiling deionized water for 1 h and immersed in 0.5 M HNO₃ (ACS Reagent, Sigma-Aldrich) for 1 h at room temperature to remove impurities. The ultrasonic spray coater (ExactaCoat, Sono-Tek) was used for the catalyst deposition with sonication set to 120 kHz, and membrane fixed on a vacuum table at 60 °C to prevent wrinkle formation. X-ray fluorescence (XRF) (Bruker M4 Tornado, Bruker) was used to ensure the loadings of 0.40 ± 0.04 mg_{Ir}·cm⁻² and 0.10 ± 0.02 mg_{Pt}·cm⁻².

In-house modified single cell electrolyzer hardware was used for electrolyzer testing. A platinum-coated single parallel channel titanium flow field was used at the anode, and a graphite single serpentine flow field was used at the cathode. The active area of the cell was set to 5 cm² using gaskets. Tape casted and commercial PTLs were used for the anode, and a carbon gas diffusion layer without an MPL (Toray 120) with PTFE content of 5% was used for cathode. Ethylene tetrafluoroethylene (ETFE) gaskets were used for both compartments, and the thicknesses were appropriately chosen to achieve 30% compression in the gas diffusion layer. The electrolyzer cell was torqued up to 4.5 Nm prior to operation.

A multichannel potentiostat (VSP 300, Biologic) with 20 A booster was used for electrochemical measurements. Heated deionized water at 80 °C was fed to the anode side at a flow rate of 100 mL·min⁻¹, and the cathode inlet was plugged. A set of cartridge heaters were used to maintain the electrolyzer temperature at 80 °C.

The electrolyzer performance was evaluated via a series of electrochemical protocols. After cell assembly, the electrolyzer underwent cyclic voltammetry (CV) conditioning of 30 cycles at a scan rate of 50 mV s⁻¹ between 1.2 V and 2 V at the operating condition (80 °C, 100 ml·min⁻¹). Second, three galvanostatic polarization curves were recorded by holding at various constant currents over a period of 130 s. The averaged potential over the last 30 s of the final polarization curve was shown as the polarization curve in this work. Galvanostatic electrochemical impedance spectroscopy (EIS) was used to capture impedance spectra at each current step of the polarization curve, with frequency range of 1 MHz to 100 mHz. The amplitude of the applied AC current was optimized for the in-house test station, so it ensures a sufficient signal to noise ratio while maintaining a leaner system response. Lastly, the iridium CV was measured from 0.05 V to 1.2 V at scanning rates of 25, 50, 75, 100, and 125 mV·s⁻¹ at operating conditions, with liquid DI water at the anode, and fully humidified H₂ flowing in the cathode at 100 ml·min⁻¹.

The overpotential breakdown was performed to analyze the ohmic, kinetic, and mass transport losses occurring in the

electrolyzer. First, the ohmic overpotential was obtained using the following equation:

$$\eta_{ohmic} = i \cdot HFR \quad [1]$$

where η_{ohmic} is the ohmic overpotential [V], i is the applied current density [A·cm⁻²], and HFR is the high frequency resistance [Ω ·cm⁻²]. Second, the kinetic overpotential, η_{kin} , was obtained by using the Tafel approximation, with an assumption that kinetics are solely governed by the oxygen evolution reaction:

$$\eta_{kin} = b \cdot \log\left(\frac{i}{i_0}\right) \quad [2]$$

where b is the measured Tafel slope [V·decade⁻¹] and i_0 is the apparent exchange current density of the electrolyzer. Third, the reversible cell potential was calculated based on the literature:³³

$$E_{rev}^0 = 1.2291 - 0.0008456 \cdot (T - 298.15) \quad [3]$$

where T is the operating temperature [K]. Finally, the residual overpotential, η_{mc} , was obtained by subtracting reversible cell potential, ohmic overpotential, kinetic overpotential from the measured cell potential.

Synchrotron X-ray computed tomography (CT).—Synchrotron X-ray computed tomography (XCT) was performed at the Advanced Light Source (ALS) Beamline 8.3.2 at Lawrence Berkeley National Laboratory. 100% whitebeam with peak energy greater than 50 keV was used to image the PTLs. Projections were collected over a rotation of 180°. The exposure time was 200 ms. The 3D reconstructions were performed using TomoPy, and the reconstructed images were segmented with an in-house developed code based on Otsu's thresholding. The pixel resolution obtained was 0.65 μm·pixel⁻¹.

Results and Discussion

Single layer structures.—Several details of PTL fabrication were maintained constant, to allow analysis of the impact of particle size, poreformer size, and addition of an MPL. Our previous work utilized <44 μm Ti powder sintered at 1000 °C, and found that a poreformer size of 60 μm and Ti: poreformer ratio of 60:40 vol% provided the best performance in a PEMWE cell.³⁰ Here, as baseline conditions, we kept the same Ti:poreformer ratio and poreformer size, and increased the sintering temperature to 1050 °C to increase PTL strength.

To understand the correlation of PTL structural properties to electrochemical performance, we first explored the impact of titanium starting powder sizes. The three different Ti powder sizes are ~5, <45, and <75 μm, and poreformer sizes are 10, 30, and 60 μm. The structural morphology of these materials is shown in Fig. S1. The tape casting process was tuned to provide precision control of layer thickness (Fig. S2), enabling a head-to-head comparison of various starting powders. The PTLs fabricated from three different Ti powder sizes are shown in Figs. 2a–2c. The PTL fabricated from ~5 μm Ti powder provides more uniform interfaces that would likely enlarge the contacting surface with the catalyst layer. Moreover, the pores formed by the poreformers are more uniformly dispersed throughout the PTL. As foreshadowed by the PTL morphology, the electrochemical analysis performed on the electrolyzers assembled with the fabricated PTLs revealed that PTLs tapecasted from smaller Ti powder size also enhances performance (Fig. 2d). Within the three different Ti powder sizes, 95 mV difference is observed at 4 A·cm⁻². Electrolyzer performance improved when smaller Ti powder sizes are used to tapecast the PTL. The breakdown analysis of ohmic, kinetic, and residual overpotentials are as shown in Figs. 2e–2g. The PTL fabricated from ~5 μm Ti powder resulted in the lowest contact resistance as

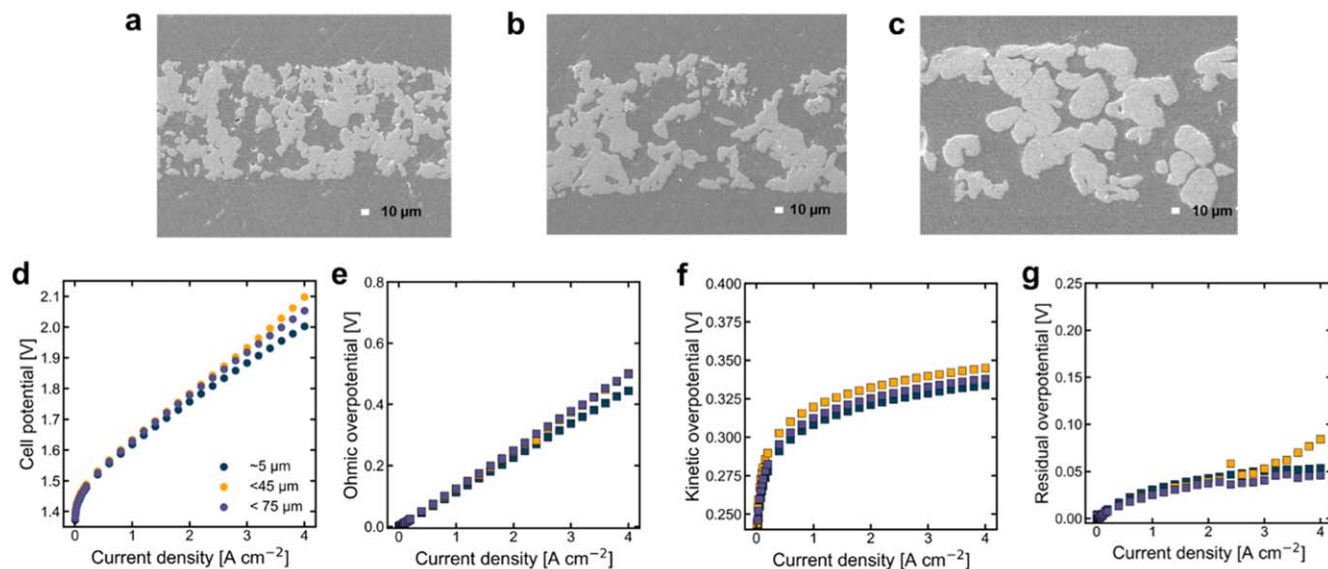


Figure 2. Morphology and performance of single layer porous transport layers fabricated from three different titanium powder sizes. The cross sectional images of PTLs fabricated from Ti powders with particle size of (a) $\sim 5 \mu\text{m}$, (b) $<45 \mu\text{m}$, and (c) $<75 \mu\text{m}$. (d) Polarization curve, (e) ohmic overpotential, (f) kinetic overpotential, and (g) residual overpotential of the PTLs.

indicated by the ohmic overpotential, while the other two larger Ti powder sizes had similar ohmic overpotentials. For kinetics, smaller Ti powder enhanced catalyst utilization leading to a decrease in kinetic overpotential. This observation agrees with the literature.²² Residual overpotentials of the three PTLs exhibited similar behavior, except at higher current densities where the residual overpotential increased for the PTL fabricated from the largest Ti powder. This is attributed to larger interfacial pores formed due to the intrinsic nature of large particles, as seen in Fig. 2c. After assessing the three different Ti powder sizes, we have downselected the $\sim 5 \mu\text{m}$ Ti powder to be used for following fabrication of MPLs.

Utilizing the fine $\sim 5 \mu\text{m}$ Ti powder, we prepared a variety of single and double layer MPL structures. Note that thick single layers are considered to be MPLs here, due to their fine structure. The impact that the pores have on MPLs was explored by varying the poreformer diameter. Four single layer MPLs were fabricated with different poreformer sizes: $0 \mu\text{m}$ (no poreformer added), $10 \mu\text{m}$,

$30 \mu\text{m}$, $60 \mu\text{m}$ (Figs. 3a–3d) and compared to commercial sintered Ti PTL (Fig. 3e). Cross sectional images show that pores in the MPL can be precisely tuned with the tape casting method, by selecting the appropriate poreformer size. Top-view SEM images of the fabricated MPLs are as shown in Fig. S4, where large PMMA particles result in large pores at the surface. The polarization curves and breakdown analysis measured for these PTLs are shown in Figs. 3f–3i. Here, we report how the pores of the MPL play a pivotal role in performance of PEM water electrolyzers. When operating with a single layer MPL without any poreformer, the electrolyzer demonstrates poor performance, and fails to maintain $3 \text{ A}\cdot\text{cm}^{-2}$. Although the kinetic overpotential remains comparable to that of other single layer MPLs and commercial sintered Ti PTL, notable increases in ohmic and residual overpotentials are evident as current density increases. This phenomenon is attributed to insufficient gas removal, impacting mass transport and also causing membrane dehydration. This result highlights that sufficient porosity is essential in fabrication of MPLs.

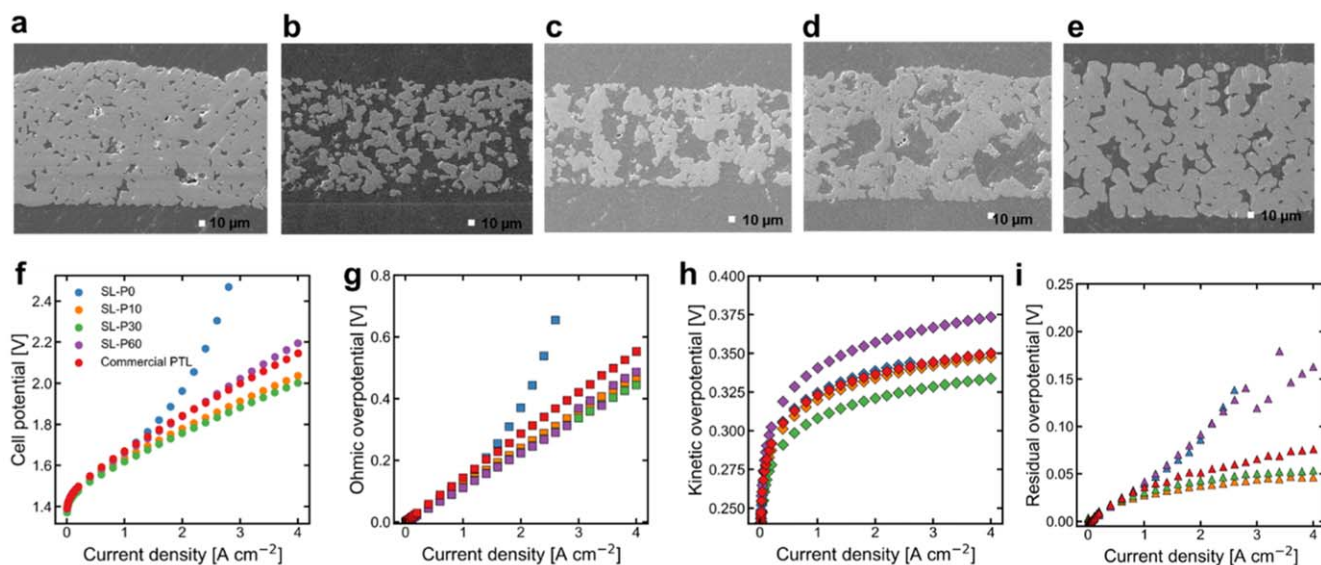


Figure 3. The performance and morphology of single layer microporous layers with varying pore sizes. The cross sectional images of single layer (SL) MPLs fabricated with (a) no pore former, (b) $10 \mu\text{m}$ pore former, (c) $30 \mu\text{m}$ pore former, (d) $60 \mu\text{m}$ pore former, and (e) commercial sintered Ti Powder PTL. (f) Polarization curve, (g) ohmic overpotential, (h) kinetic overpotential, and (i) residual overpotential.

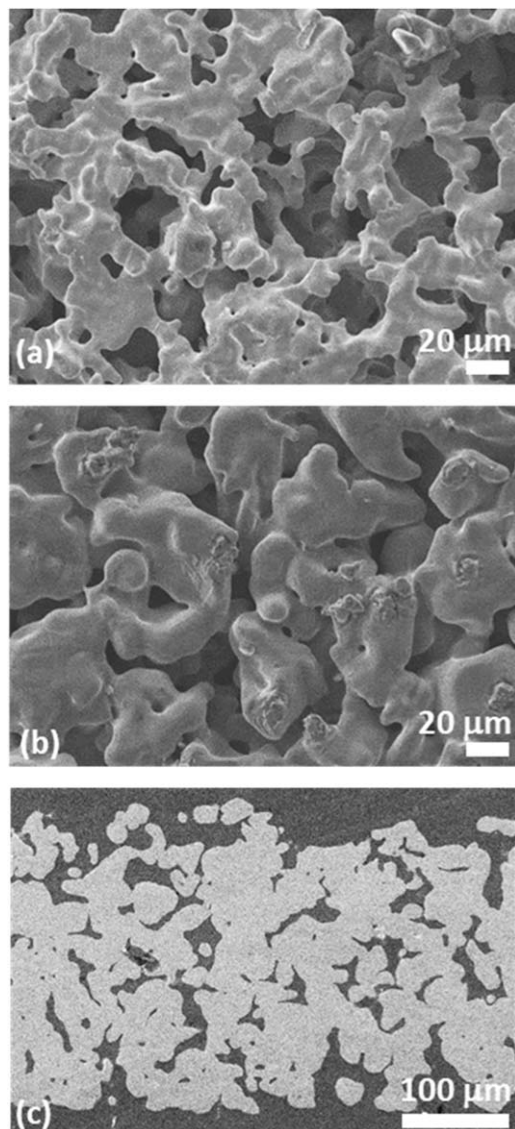


Figure 4. MPL wet-cast onto commercial PTL. SEM images of (a) MPL surface, (b) commercial sintered PTL surface, and (c) polished cross-section with the MPL layer on the top. Note that the wet MPL layer wicked into the PTL before drying, preventing a clear MPL layer from being formed.

With poreformers mixed into the MPL, significant performance improvement is observed. Specifically, single layer MPLs fabricated with $10\ \mu\text{m}$ and $30\ \mu\text{m}$ PMMA sizes outperformed the commercial sintered Ti PTL by $109\ \text{mV}$ and $142\ \text{mV}$ at $4\ \text{A}\cdot\text{cm}^{-2}$, respectively. The major contributor to this substantial enhancement is ohmic overpotential. Finer Ti powders reduce contact resistance and maintaining electrical conductivity, and all single layer MPLs with poreformers led to reduction in the high frequency resistance. The MPL featuring $30\ \mu\text{m}$ PMMA demonstrated the lowest kinetic overpotential, which is attributed to the constructive synergy achieved through effective gas removal and improved interfacial contact. Residual overpotential is lower for $10\ \mu\text{m}$ and $30\ \mu\text{m}$ poreformers, but was higher for $60\ \mu\text{m}$. For this MPL with the largest poreformer size, the pores are not well-dispersed throughout the MPL, and large regions of the MPL are free of poreformer thereby increasing mass transport resistance similarly to the poreformer-free sample. The porosity profiles of the single layer MPLs are shown in Fig. S7, where the variation of porosities between the SL-P10, SL-P30, and SL-P60 are within 4 percentage points. However, the porosity near the catalyst layer is lower for MPLs with larger PMMA because larger PMMA tends to concentrate in the

middle of the microporous layer during drying process. This may contribute to higher performance of SL-P30 compared to SL-P10. For the $\sim 5\ \mu\text{m}$ Ti powder size, $30\ \mu\text{m}$ poreformer provides the best performance, and these particle sizes are selected for fabrication of bilayer structure MPLs. This combination is aligned with the numerical study of Xu et al., which found that the average pore size of the PTL must be larger than $10\ \mu\text{m}$.³⁴

Addition of MPLs to commercial baseline PTLs.—As a first trial, an MPL layer was added to several of the tape cast PTL layers. Thin MPL tapes were initially prepared with $5\ \mu\text{m}$ Ti and $10\ \mu\text{m}$ PMMA particles, using the same solvent and binder system as the PTL layers. The green MPL and PTL tapes were easily laminated together by warm pressing, and co-sintered to produce flat MPL/PTL structures, Fig. S2. We observed that incorporating a higher-performing MPL at the interface between the catalyst layer and the low-performing PTL substrate resulted in performance enhancement, as illustrated in Fig. S5. This suggests that the application of MPLs can be employed to leverage the use of affordable and easily manufacturable PTL substrates, such as those available commercially.

These observations motivated us to apply an MPL to commercial baseline PTLs, as these show relatively low performance compared to the best single layer PTLs, and therefore can be expected to benefit from addition of an MPL. An MPL with $5\ \mu\text{m}$ Ti and $30\ \mu\text{m}$ PMMA particles was downselected, based on the excellent performance of the comparable single layer MPL discussed above, Fig. 3. Applying the MPL layer to pre-sintered commercial PTLs, however, was quite challenging. The initial approach was to prepare a free-standing MPL layer and place it between the MEA and PTL during cell assembly. Free-standing MPLs were prepared with a thickness of approximately $40\ \mu\text{m}$, Fig. S2d. However, these MPLs proved too weak for testing and failed during the catalyst deposition and cell assembly process leading to low electrochemical performance. This approach was not pursued further, and instead we assessed various methods to mechanically support the MPL by sinter-bonding it to the PTL. First, the MPL tape casting slurry was cast directly onto a commercial PTL structure. Due to large pores in the PTL and relatively low viscosity of the MPL slurry, the MPL seeped into the PTL structure. After sintering, a clear MPL layer was absent, and the MPL particles were barely visible in the surface of the PTL, Fig. 4. To overcome this issue, we attempted to sinter-bond an MPL layer to the PTL. The MPL was tape cast, dried, and laminated to the PTL. The bilayer stack was sintered with a dead weight on top to promote contact and bonding between the layers. In some regions, good bonding was achieved, but in other regions no bonding occurred and the MPL could be easily peeled off with minimal force, Fig. 5.

Finally, to promote MPL-PTL bonding over the entire area, binder was added to the PTL. The bare PTL was immersed in the tapecasting binder solution and then dried overnight. Then the green MPL and binder-coated PTL layers, both containing the same binder, were laminated together at a moderate pressure to bond both layers without damaging the PTL structure. The bilayer was then sintered at $850\ ^\circ\text{C}$, as this temperature was deemed a suitable compromise between achieving good mechanical strength and electrical contact, and the prevention of shrinkage cracks in the MPL at higher temperatures. Binder-coating the PTL and the warm MPL-PTL lamination process successfully resulted in a well-interconnected interface between a distinct MPL layer and the commercial PTLs, Fig. 6.

The electrochemical performance of the MPL/commercial bare PTL bilayers is shown in Fig. 7. Addition of the tape casted MPL in between the catalyst layer and both types of commercial PTL led to notable performance improvement. For the BL-P30-Fiber (bilayer, PMMA $30\ \mu\text{m}$ MPL on Fiber PTL) structure, electrolyzer overpotential was reduced by $165\ \text{mV}$ at $4\ \text{A}\cdot\text{cm}^{-2}$ compared to the commercial sintered Ti fiber PTL. Similarly, the BL-P30-Powder structure reduced overpotential by $103\ \text{mV}$ compared to the commercial Ti sintered powder PTL. The use of the MPL closed

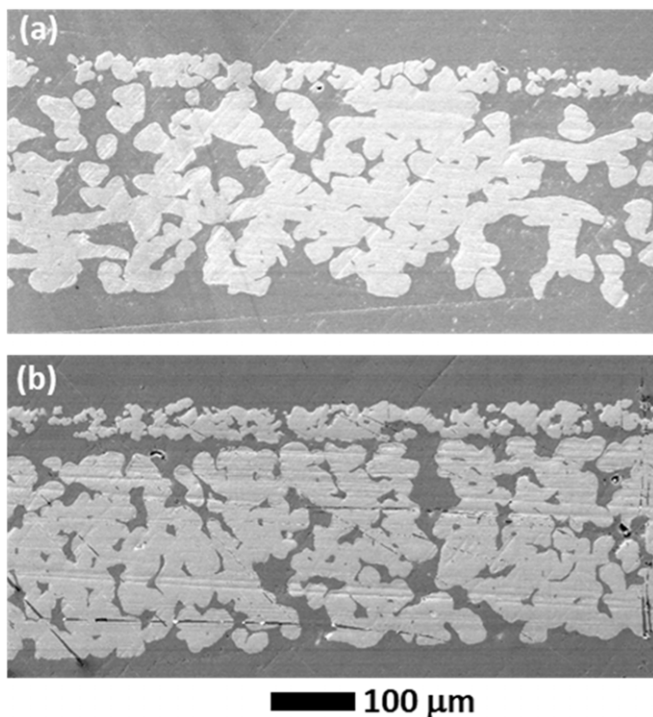


Figure 5. MPL tape laminated to bare commercial PTL. SEM cross-section image of MPL (top layer) bonded to Bekaert fiber 2GDL10–0.25 PTL, after laminating the MPL tape to the bare PTL and sintering the bilayer structure. Bonding was inhomogeneous and some regions (a) were bonded well while other regions (b) were not bonded at all.

the gap between the commercial Ti powder and fiber PTLs by 45 mV. This finding is noteworthy as use of MPLs may enable the use of less expensive PTL structures for large-scale manufacturing. The majority of the improvement in performance stemmed from reduction in ohmic and kinetic losses as shown in the voltage breakdowns (Figs. 7b–7d). With the MPLs, the large pores that are usually present at the CL/PTL interface are replaced by numerous smaller pores, which prevents deformation of the membrane and catalyst layer thereby enhancing catalyst utilization. In fact, our synchrotron X-ray computed tomography (CT) results (Fig. 8) reveal that the tape casted MPLs introduce higher porosity near the CL/PTL interface (Fig. 8e) and yet these pores are much smaller compared to commercial PTLs (Fig. 8f). As a result, the Tafel slopes reduce with addition of the MPL, from 54.3 to 44.0 mV dec⁻¹ for commercial sintered Ti fiber PTL and from 47.4 to 44.3 mV dec⁻¹ for commercial Ti powder PTL. A similar observation has been made by Schuler et al.,^{22,29} where lower Tafel slope was observed for their MPLs compared to the bare PTL substrate. The mass transport loss of MPL/PTL bilayers remained similar to the commercial sintered Ti powder PTL for the range of current densities tested in this work, Fig. 7d. This is attributed to the minimal change in the tortuosity and permeability of the bilayers even though the average pore sizes decreased by at least 10% relative to the bare PTLs (Table I). The BL-P30-Powder slightly underperforms the SL-P30 single layer MPL (Fig. S8), and we hypothesize that this is due to the lower porosity for the commercial Powder layer relative to the SL-P30 single layer (Fig. S7).

Phase inversion structure development.—Further manipulation of the pore structure was carried out using the phase inversion tape casting process. The resulting structure may be considered as a combined MPL/PTL prepared in a single process. The phase inversion process creates finger-like pores when the solvent in a slurry of particles and binder counter-diffuses with a non-solvent

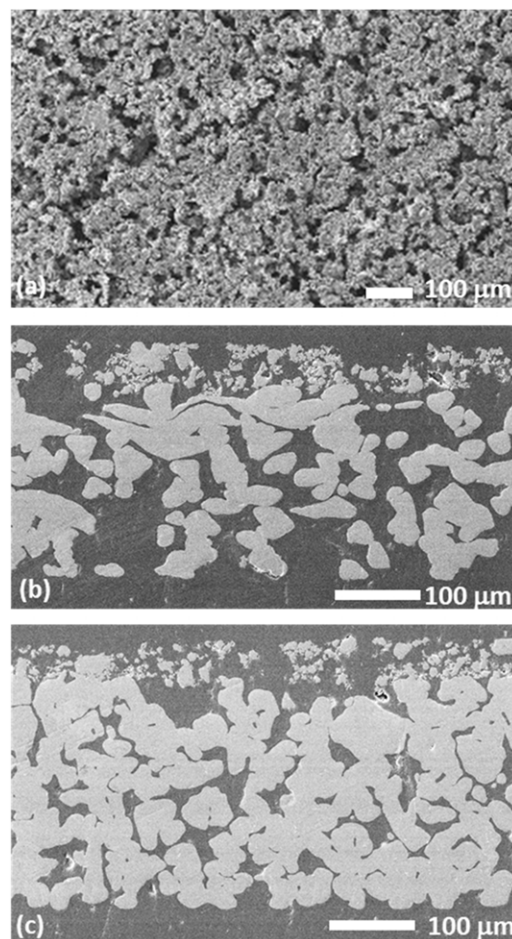


Figure 6. MPLs laminated on commercial PTL layers pre-coated with binder. SEM images of (a) MPL surface, and polished cross-sections of MPL well bonded to (b) Bekaert fiber PTL and (c) Mott sinter PTL.

liquid in contact with the surface of the slurry. A common phase inversion system is NMP as the solvent, and water as the non-solvent. The phase inversion structure is characterized by low-tortuosity elongated pores running through the plane of a film or sintered layer. When phase inversion follows tape casting, the bottom face of the tape on the casting substrate remains relatively dense, while the upper portion of the tape exposed to the non-solvent liquid becomes highly porous. The denser region supports the membrane and provides intimate contact with the catalyst layer, while the elongated pores provide a path for bubble removal and liquid flow with minimal mass transport resistance.

Preparing a tape cast phase inversion structure with Ti powder has several challenges. The typical binders used in phase inversion casting are not compatible with Ti sintering, as they are not easily removed in Ar atmosphere. We avoid very fine Ti for safety reasons, and the 5 μm Ti particles used here are larger than the sub-micron particles often used for phase inversion casting. The elongated pores tend to close down to a smaller diameter near the top of the layer, creating a structure like a *cenote* sinkhole, with limited pore access at the PTL/bipolar plate interface. To overcome these challenges, we modified the phase inversion materials and processing approach. QPAC-40 was identified as a suitable binder that works with the NMP/water phase inversion solvent/non-solvent system and burns off in Ar at low temperature ~300 °C (see Fig. S3 and associated discussion for more details). The pore shape was controlled through two processing modifications. First, the temperature of the water used for phase inversion was reduced. Using warm water failed to produce the desired structure, but using an ice bath to cool the water

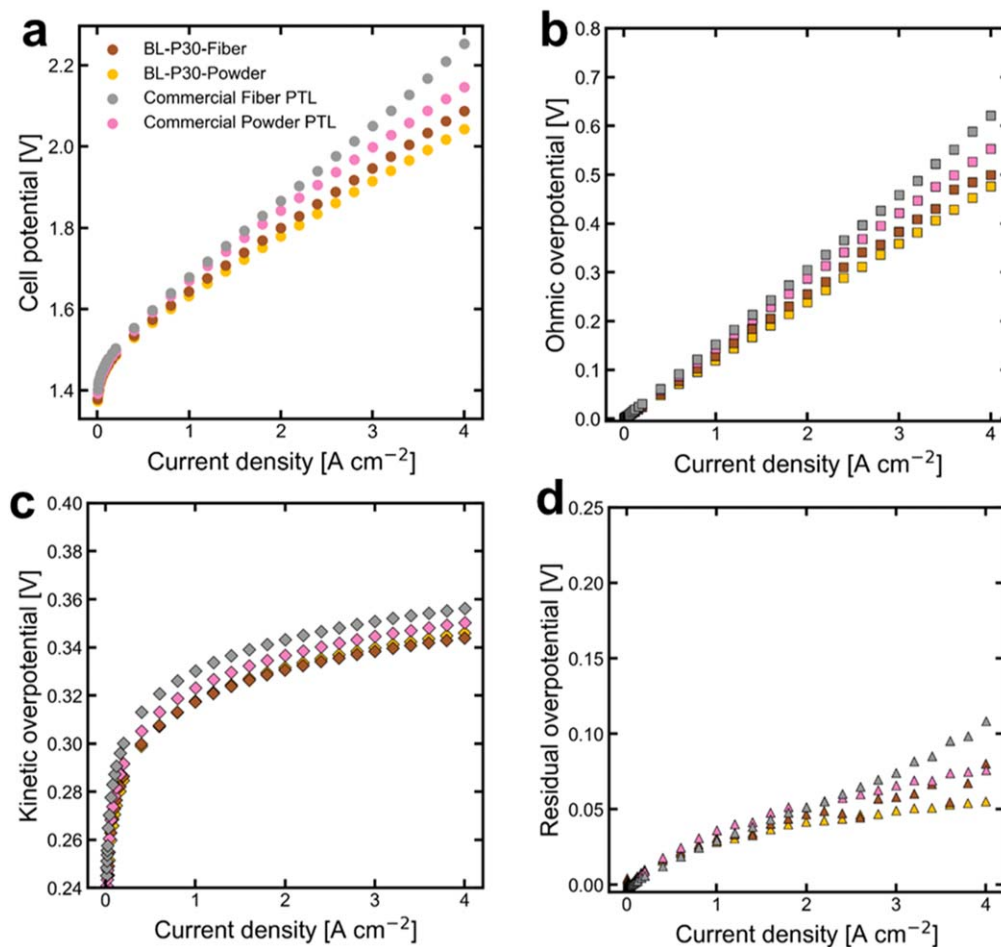


Figure 7. The performance of bilayer (BL) MPL/PTL structures compared to commercial PTLs. (a) Polarization curve, (b) ohmic overpotential, (c) kinetic overpotential, and (d) residual overpotential.

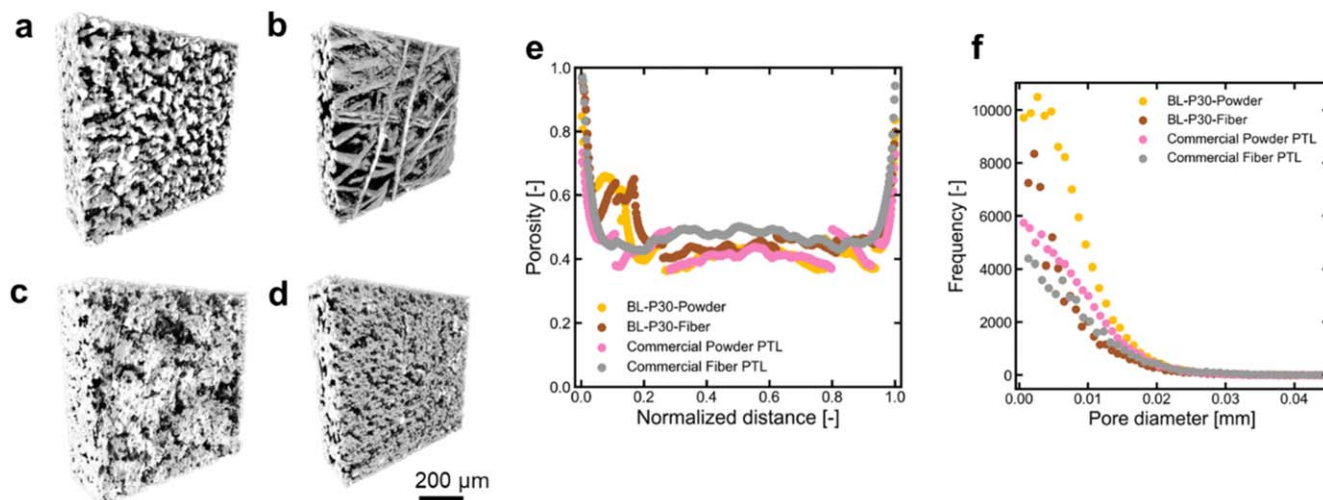


Figure 8. Synchrotron X-ray CT analysis of the bilayer MPLs on commercial PTLs. 3D reconstruction of (a) commercial sintered Ti Powder PTL, (b) commercial sintered Ti Fiber PTL, and MPL on commercial (c) sintered Ti powder and (d) commercial Ti fiber PTLs. (e) Porosity through the thickness and (f) pore size distributions of the structures.

to ~0 °C generated the expected elongated pores, Figs. S6a, S6b. Second, a sacrificial layer of PMMA was cast on top of the Ti layer before submerging this bi-layer structure in water. The smaller pore diameter near the top of the pore therefore occurred within the PMMA layer, which burned off during sintering, revealing the large

pores in the Ti layer. This moderately increased the pore size at the top surface of the final sintered Ti structure, Fig S6c.

Based on this modified phase inversion tape casting process, a Ti structure was fabricated with a thin layer of <20 μm pores and a thick layer with large elongated pores with 50 to 100 μm diameter,

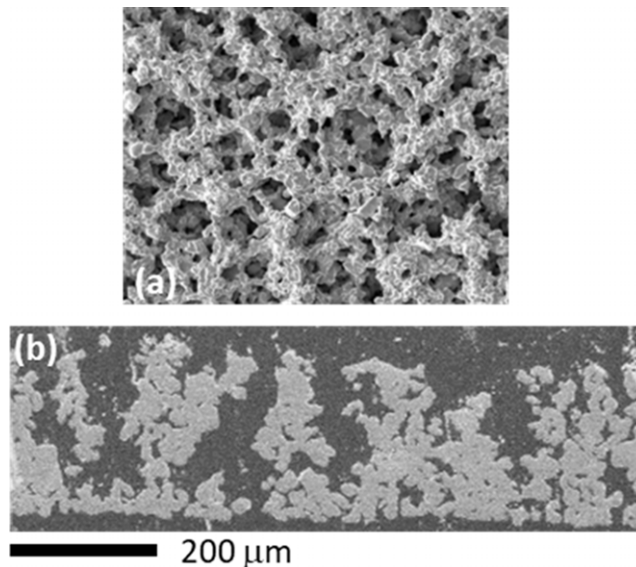


Figure 9. Phase inversion structure. SEM images of (a) top porous surface and (b) polished cross-section of sintered PTL structure prepared using a sacrificial PMMA layer cast on top of the Ti layer before submerging both in a 0 °C water bath for phase inversion.

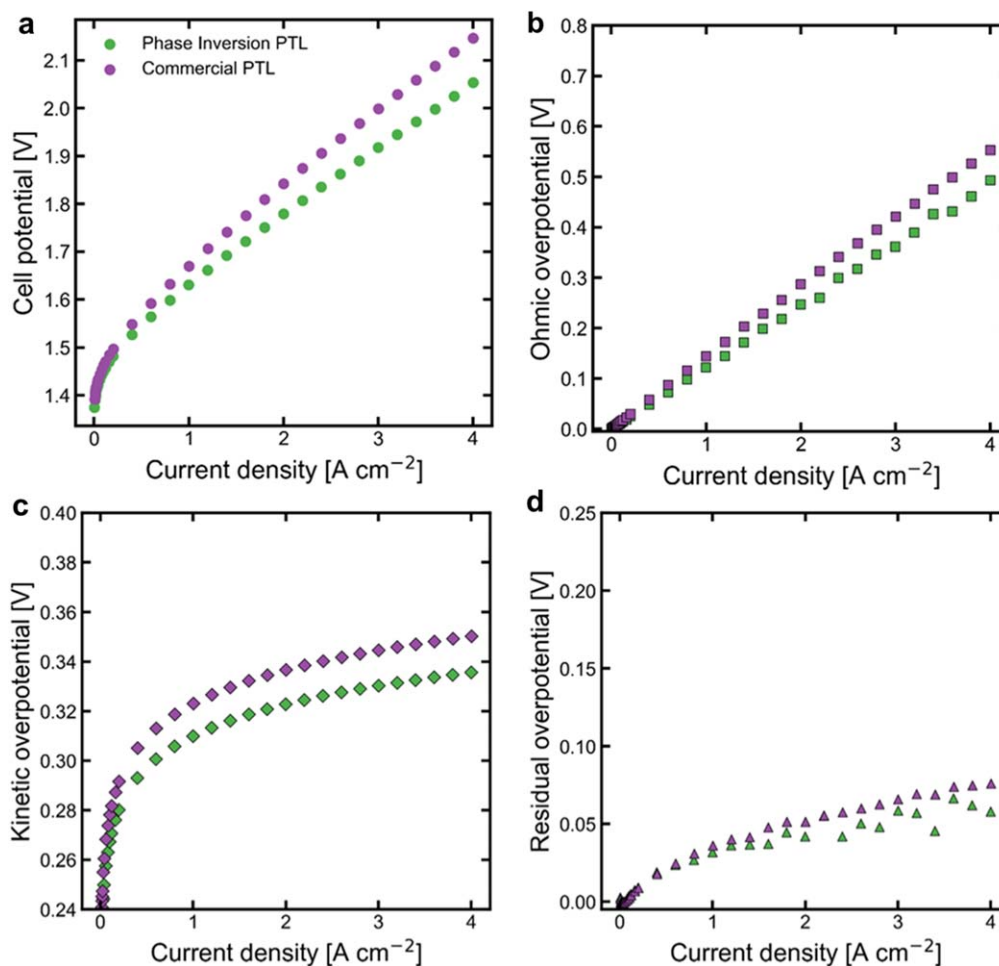


Figure 10. The performance of the phase inversion PTL compared with commercial sintered Ti powder PTL. (a) Polarization curve, (b) ohmic overpotential, (c) kinetic overpotential, and (d) residual overpotential.

Fig. 9. During cell assembly, the less porous face contacted the catalyst-coated membrane, and the highly porous face contacted the bipolar plate.

The phase inversion PTL exhibited superior performance compared to the commercial Ti sintered powder PTL. As shown in Fig. 10, the phase inversion PTL reduced the electrolyzer voltage by

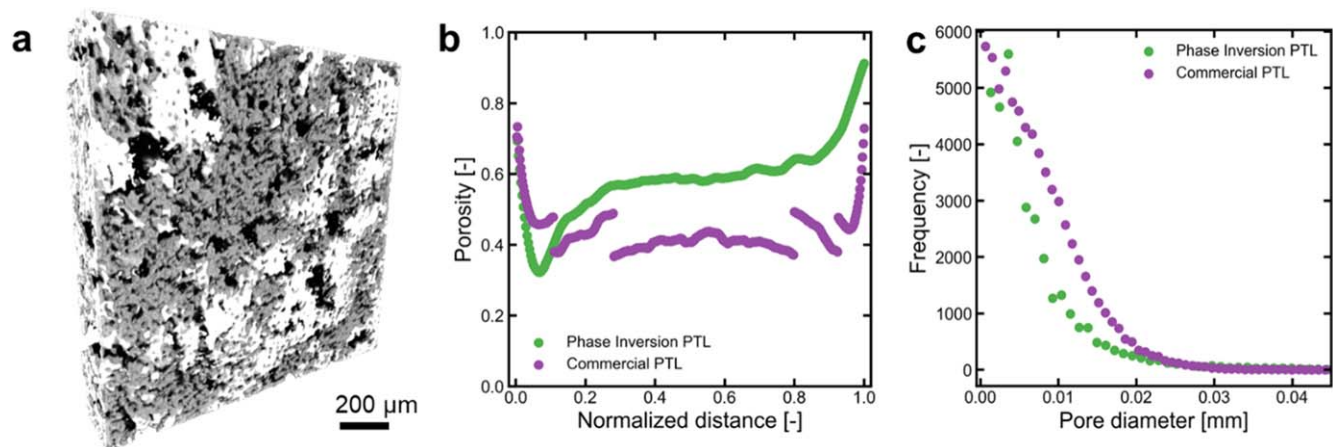


Figure 11. Synchrotron X-ray CT analysis of the phase inversion PTL. (a) 3D reconstruction of phase inversion PTL. (b) Porosity through the thickness and (c) pore size distributions of the phase inversion PTL and commercial sinter PTL.

Table I. Pore structure of the microporous layers obtained from synchrotron X-ray CT. The average pore size, tortuosity, and permeability in the thickness direction acquired from the X-ray CT data.

	Average pore size [μm]	Tortuosity [-]	Permeability [$\times 10^{-12} \text{ m}^2$]
BL-P30-Powder	60	2.61	2.64
BL-P30-Fiber	68	2.41	7.64
Commercial powder PTL	67	2.59	3.61
Commercial fiber PTL	85	2.37	8.54
Phase inversion PTL	73	1.79	7.33

92 mV at $4 \text{ A}\cdot\text{cm}^{-2}$ from that of commercial Ti sintered powder PTL. The phase inversion structure significantly lowers ohmic and kinetic overpotentials, and it is speculated that the finger-like structure of the phase inversion PTL promotes the effective gas removal during electrolysis. This effective gas removal is similar to observation made from the literature, where patterned through-pores, which are similar to the finger-like structure, led to increased gas rip-off frequency, thereby significantly enhancing the mass transport.²⁸ Moreover, synchrotron X-ray CT data in Fig. 11 shows that the phase inversion PTL has lower porosity next to the catalyst layer but has a gradual increase in porosity in the thickness direction. The porosity profile is distinctively unique from that of bilayer MPL/PTL structures, and is similar to the PTLs investigated through stochastic models in the literature.^{19,20} In fact, a previous study showed that gradient porosity with low porosity adjacent to the catalyst layer enhances mass transport, as evident from neutron radiography.²¹ Hence, the porosity gradient and low tortuosity of the phase inversion PTL direct towards enhanced transport, and poses a new paradigm in MPL/PTL design. When the performance of the PTLs and MPLs are evaluated together (Fig. S8), the three-best performing MPLs and PTLs are the single layer MPL with PMMA $30 \mu\text{m}$ (SL-P30), bilayer MPL with PMMA $30 \mu\text{m}$ coated over commercial Ti powder PTL, and phase inversion PTL. This suggests that further optimization of the phase inversion tape casting process may be fruitful.

Conclusions

In this work, tape casting is used as a scalable method to fabricate MPLs for PEM water electrolyzers. Tape casting enables the use of various titanium particle sizes, and grants fine control of the pore structure by mixing in poreformers. Three different types of MPL/PTL structures have been fabricated: (i) single layer PTLs and MPLs, (ii) bilayer MPL/PTLs, and (iii) low tortuosity phase inversion tape casted layers. Comprehensive testing of the single layer MPLs demonstrated that sufficient pore sizes between 10 to $30 \mu\text{m}$ are required for effective gas removal within the MPLs, and

an MPL without any poreformer led to drastic increase in overpotentials. We also revealed that having an effective MPL enhances electrolyzer performance regardless of the PTL substrate used, which opens up room for cost reduction of clean hydrogen. Lastly, we investigated the low tortuosity layers fabricated from phase inversion tape casting, which resulted in significantly reduced overpotential relative to commercial baseline PTL. Our research provides guidance on the design and fabrication processes for future-generation PTLs, outlining how MPLs should be developed and constructed.

Acknowledgments

The authors acknowledge the Department of Energy–Office of Energy Efficiency and Renewable Energy–Fuel Cell Technologies Office (DOE-EERE-FCTO) and the H2 from the Next-generation Electrolyzers of Water (H2NEW) consortium for funding under Contract Number DE-AC02–05CH11231. This research used resources of the Advanced Light Source (ALS), a DOE Office of Science User Facility under contract no. DEAC02–05CH11231. We are grateful to Dr Dula Parkinson for help with micro-tomography measurement at Beamline 8.3.2 of ALS.

This document was prepared as an account of work sponsored by the United States Government. While this document is believed to contain correct information, neither the United States Government nor any agency thereof, nor the Regents of the University of California, nor any of their employees, makes any warranty, express or implied, or assumes any legal responsibility for the accuracy, completeness, or usefulness of any information, apparatus, product, or process disclosed, or represents that its use would not infringe privately owned rights. Reference herein to any specific commercial product, process, or service by its trade name, trademark, manufacturer, or otherwise, does not necessarily constitute or imply its endorsement, recommendation, or favoring by the United States Government or any agency thereof, or the Regents of the University of California. The views and opinions of authors expressed herein do

not necessarily state or reflect those of the United States Government or any agency thereof or the Regents of the University of California. This manuscript has been authored by an author at Lawrence Berkeley National Laboratory under Contract No. DE-AC02-05CH11231 with the U.S. Department of Energy. The U.S. Government retains, and the publisher, by accepting the article for publication, acknowledges, that the U.S. Government retains a non-exclusive, paid-up, irrevocable, world-wide license to publish or reproduce the published form of this manuscript, or allow others to do so, for U.S. Government purposes.

ORCID

Jason K. Lee  <https://orcid.org/0000-0003-1929-0864>
Fengyu Shen  <https://orcid.org/0000-0003-3818-176X>

References

1. B. Pivovar, N. Rustagi, and S. Satyapal, *Electrochem. Soc. Interface*, **27**, 47 (2018).
2. D. A. Cullen, K. C. Neyerlin, R. K. Ahluwalia, R. Mukundan, K. L. More, R. L. Borup, A. Z. Weber, D. J. Myers, and A. Kusoglu, *Nat. Energy*, **6**, 462 (2021).
3. R. Nayak-Luke, R. Bañares-Alcántara, and I. Wilkinson, *Ind. Eng. Chem. Res.*, **57**, 14607 (2018).
4. H. Zhang, L. Wang, J. Van herle, F. Maréchal, and U. Desideri, *Appl. Energy*, **259**, 114135 (2020).
5. H. Muslemeni, X. Liang, K. Kaesehage, F. Ascui, and J. Wilson, *J. Clean. Prod.*, **315**, 128127 (2021).
6. K. Rechberger, A. Spanlang, A. Sasiain Conde, H. Wolfmeir, and C. Harris, *Steel Res. Int.*, **91**, 2000110 (2020).
7. A. Sasiain, K. Rechberger, A. Spanlang, I. Kofler, H. Wolfmeir, C. Harris, T. Bürgler, and D. A. Sasiain, *BHM Berg- und Hüttenmännische Monatshefte*, **165**, 232 (2020).
8. M. H. Ali Khan, R. Daiyan, P. Neal, N. Haque, I. MacGill, and R. Amal, *Int. J. Hydrogen Energy*, **46**, 22685 (2021).
9. R. Hren, A. Vujanović, Y. Van Fan, J. J. Klemeš, D. Krajnc, and L. Čuček, *Renew. Sustain. Energy Rev.*, **173**, 113113 (2023).
10. M. Carmo, D. L. Fritz, J. Mergel, and D. Stolten, *Int. J. Hydrogen Energy*, **38**, 4901 (2013).
11. T. Schuler, T. J. Schmidt, and F. N. Büchi, *J. Electrochem. Soc.*, **166**, F555 (2019).
12. T. Schuler, R. De Bruycker, T. J. Schmidt, and F. N. Büchi, *J. Electrochem. Soc.*, **166**, F270 (2019).
13. Z. Kang et al., *Int. J. Hydrogen Energy*, **43**, 14618 (2018).
14. Z. Kang, J. Mo, G. Yang, S. T. Retterer, D. A. Cullen, T. J. Toops, J. B. Green, M. M. Mench, and F. Y. Zhang, *Energy Environ. Sci.*, **10**, 166 (2017).
15. J. Mo, G. Yang, Y. Li, Z. Kang, G. Bender, B. S. Pivovar, J. B. Green, and F. Y. Zhang, *Int. J. Hydrogen Energy*, **45**, 26595 (2020).
16. J. Mo, Z. Kang, S. T. Retterer, D. A. Cullen, T. J. Toops, J. B. Green, M. M. Mench, and F. Y. Zhang, *Sci. Adv.*, **2**, e1600690 (2016).
17. X. Peng et al., *Energy Environ. Sci.*, **13**, 4872 (2020).
18. X. Peng, P. Satjaritanun, Z. Taie, L. Wiles, A. Keane, C. Capuano, I. V. Zenyuk, and N. Danilovic, *Adv. Sci.*, **8**, 2102950 (2021).
19. J. K. Lee, C. H. Lee, and A. Bazylak, *J. Power Sources*, **437**, 226910 (2019).
20. J. K. Lee and A. Bazylak, *J. Electrochem. Soc.*, **167**, 013541 (2020).
21. J. K. Lee et al., *Energy Convers. Manag.*, **226**, 113545 (2020).
22. T. Schuler, J. M. Ciccone, B. Krentscher, F. Marone, C. Peter, T. J. Schmidt, and F. N. Büchi, *Adv. Energy Mater.*, **10**, 1903216 (2020).
23. P. Lettenmeier, S. Kolb, F. Burggraf, A. S. Gago, and K. A. Friedrich, *J. Power Sources*, **311**, 153 (2016).
24. P. Lettenmeier, S. Kolb, N. Sata, A. Fallisch, L. Zielke, S. Thiele, C. A.-S. Gago, and K. A. Friedrich, *Energy Environ. Sci.*, **10**, 2521 (2017).
25. S. Stiber, N. Sata, T. Morawietz, S. A. Ansar, T. Jahnke, J. K. Lee, A. Bazylak, A. Fallisch, A. S. Gago, and K. A. Friedrich, *Energy Environ. Sci.*, **15**, 109 (2022).
26. S. Stiber et al., *Adv. Energy Mater.*, **11**, 2100630 (2021).
27. D. C. Dunand, *Adv. Eng. Mater.*, **6**, 369 (2004).
28. J. K. Lee, C. H. Lee, K. F. Fahy, P. J. Kim, K. Krause, J. M. LaManna, E. Baltic, D. L. Jacobson, D. S. Hussey, and A. Bazylak, *ACS Appl. Energy Mater.*, **3**, 9676 (2020).
29. T. Schuler, C. C. Weber, J. A. Wrubel, L. Gubler, B. Pivovar, F. N. Büchi, and G. Bender, *Adv. Energy Mater.*, **14**, 2302786 (2024).
30. J. K. Lee, G. Y. Lau, M. Sabharwal, A. Z. Weber, X. Peng, and M. C. Tucker, *J. Power Sources*, **559**, 232606 (2023).
31. R. E. Mistler, "The principles of tape casting and tape casting applications." *Ceramic Processing*, ed. R.A. Terpstra (Springer, Dordrecht) 147–173 (1995).
32. F. Shen, R. A. Jonson, D. Y. Parkinson, and M. C. Tucker, *J. Am. Ceram. Soc.*, **105**, 90 (2022).
33. S. G. Bratsch, *J. Phys. Chem. Ref. Data*, **18**, 1 (2009).
34. C. Xu, J. Wang, J. Wang, K. Yang, G. Li, W. Gao, H. Wang, and S. Zhao, *Appl. Energy*, **357**, 122541 (2024).